The Solvent Matters: Kinetic *versus* Thermodynamic Shape Control in the Polyol Synthesis of Rhodium Nanoparticles

Adam J. Biacchi and Raymond E. Schaak*

Department of Chemistry and Materials Research Institute, The Pennsylvania State University, University Park, Pennsylvania 16802, United States

ABSTRACT The polyol process is one of the most common methods for synthesizing metal nanoparticles with controlled shapes and sizes due to its wide applicability and ease of use. These nanostructures often have unique morphology-dependent properties that are useful in a range of applications, including catalysis, plasmonics, and medical diagnostics and therapeutics. While many variations of the polyol process have been developed to produce shape-controlled nanoparticles, there has been no systematic investigation that defines the influence of the solvent on the shape and uniformity of the product. Here we show that proper selection of the polyol solvent can be used to manipulate the metal nanoparticle morphology. Each polyol has a different oxidation potential which, along with the metal reagent, defines the temperature at which particle formation takes place. For a given system, particle growth will vary between a kinetic and thermodynamic regime depending on the thermal conditions, which can be modulated through selection of the appropriate solvent. This strategy, which is demonstrated for the catalytically relevant rhodium system, facilitates the high-yield synthesis of monodisperse rhodium nanoparticles with shapes that include icosahedra, cubes, triangular plates, and octahedra.

KEYWORDS: rhodium nanoparticles · nanoparticle synthesis · polyol process · shape controlled-nanoparticles

Synthetic methods that rigorously and predictably control the nanoscale morphological features of colloidal metal nanoparticles are important because their inherent catalytic,[1] optical,[2] thermal,[3] magnetic,[4] and electronic[5] properties change with variations in shape, size, composition, crystallinity, and structure. Solution-based strategies succeed at producing monodisperse colloidal nanoparticles with controllable shapes and sizes by reducing and decomposing appropriate metal reagents. Numerous experimental conditions have been found to influence the product, including the metal precursor, the reducing agent, the reaction temperature and duration, the stabilizer, added redox-active species, and any adsorbates present during synthesis.[6,7] Careful manipulation of these factors can alter the nucleation and growth processes of the reaction in a controllable manner to selectively generate nanoparticles of desired dimensions, morphologies, and exposed crystalline facets.

One of the most important applications of shape- and size-controlled metal nanoparticles is in catalysis.[8] Significant differences in catalytic activity[9] and selectivity[10] have been observed for shape-controlled metal[11] and alloy[12] nanoparticles, and these are often attributed to the presence or absence of certain crystallographic planes associated with a particular nanocatalyst shape. These exposed facets, as well as their associated atomic steps, corners, and defects, can help to improve catalytic performance by favoring the preferential adsorption of reactant species or disfavoring the adsorption of species capable of poisoning a catalytic metal.[13,14] Nanoparticle size can also influence catalytic activity,[15] selectivity,[16] and durability,[17] with the highest activity generally associated with the largest surface-to-volume ratio (*e.g.*, smallest sizes). However, in some cases, the smallest nanoparticles may be less active than their more moderately sized analogues.[18] Therefore, the ability to predictably and controllably tailor particle size along with morphology is essential for achieving optimal catalyst performance.

Among catalytic metal nanoparticles, rhodium is particularly interesting. Rh nanoparticles catalyze a diverse range of reactions, including oxidations,[19] reductions,[20] hydroformylations,[21] and cross-couplings.[22] Rhodium has a strong resistance to acids and bases and it also has a higher melting point than many other catalytically active metals, such as Pt and Au. These characteristics make Rh nanoparticles especially stable under harsh reaction conditions. While polymer-stabilized rhodium colloids have been used for catalytic applications for

* Address correspondence to schaak@chem.psu.edu.

Received for review July 16, 2011 and accepted September 3, 2011.

Published online September 21, 2011
10.1021/nn2026758

several decades,[23−25] many reports use catalysts that are largely undefined or are polydisperse in shape and size.[26−28] Compared to other noble metal systems, rhodium nanoparticles have only been synthesized as high-yield monodisperse particles for a limited number of morphologies that include cubes,[29] tetrahedra,[30] octahedra,[31] spherical[32] and dendritic[33] aggregates, concave cubes,[34] 3-fold branched particles,[35] 5-fold branched particles,[36] and hexagonal polyhedra.[37] Despite its catalytic value, there are far fewer reports of shape- and size-controlled routes to Rh nanoparticles than other noble metals such as Au,[38] Ag,[39] Pt,[40] and Pd,[41] and comprehensive studies that explicitly link reaction parameters to shape and size control have not yet been reported.

One of the most common solution-phase approaches for synthesizing Rh and other metal nanoparticles is the polyol process. To generate metal colloids, an organometallic complex or metal salt precursor is heated, often in the presence of a stabilizing agent, in a high-boiling polyalcohol that serves as both solvent and reducing agent.[42,43] Reactions are generally mild, often occurring at temperatures below 200 °C and using relatively benign reagents such as the polymeric stabilizer poly(vinyl pyrrolidone) (PVP),[44] and they generate nanoparticles that can be dispersed in polar solvents, which facilitates biological and environmental applications. Modifications to the polyol process permit the synthesis of shape- and size-controlled nanoparticles.[45,46] Many experimental variables have been studied in the polyol synthesis of shape- and size-controlled metal nanoparticles. However, despite the diversity of polyols that are commercially available, ethylene glycol is used almost exclusively, and few reports offer direct comparisons among different polyols.[47−50] Understanding the influence of the polyol solvent on the kinetics and thermodynamics of nanoparticle synthesis is critically important for expanding our ability to synthesize high-quality shape- and size-controlled nanoparticles.

In this paper, we describe a comprehensive set of systematic studies that provide important new insights into the synthesis of colloidal Rh nanoparticles using a modified polyol process. First, we elucidate the independent roles of the polyol solvent and the anionic ligand from the metal reagent in controlling the shape and uniformity of Rh nanoparticles. These studies provide empirical guidelines for the high-yield synthesis of monodisperse Rh icosahedra, cubes, and triangular plates, for which the average nanoparticle size can also be tuned. We then show that the polyol solvent defines the temperature and rate at which particles form, both of which affect shape and uniformity. We also show that the polyol solvent can influence whether particles form under largely thermodynamic or kinetic control to yield equilibrium or nonequilibrium shapes, respectively. Collectively, this demonstrates that judicious choice of the appropriate polyol solvent can serve as a powerful synthetic lever for predictably selecting and fine-tuning nanoparticle morphology. As an application of these insights, monodisperse nanoparticles of Rh octahedra are synthesized in high yield. These results, which emerge from an exhaustive set of illustrative experiments, effectively merge the capabilities of simple one-pot heat-up methods with those of hot-injection processes that use a syringe pump to manipulate kinetics by continuously delivering controlled amounts of reagents.

RESULTS AND DISCUSSION

Shape-Controlled Rhodium Nanoparticles. Several sets of carefully designed experiments allowed us to elucidate and understand the competing roles of the ligand and polyol solvent in defining the morphologies of Rh nanoparticles. For these studies, the amounts and concentrations of Rh reagent, PVP stabilizer, and polyol solvent were held constant, and all reactions were carried out under Ar to limit any oxidative etching effects.[51] Use of a one-pot heat-up method allowed us to separate the nucleation and growth steps by modulating temperature. Using a procedure that is similar to previously reported polyol methods,[11,29,44] the temperature was gradually increased until reduction was visually apparent (*e.g.*, formation of a dark brown-colored solution), held at this temperature for 15 min to generate a high concentration of seeds, increased by 30−50 degrees (determined based on optimization studies for each system) to initiate growth by an *in situ* seed-mediated mechanism, held at this temperature for 1.5 h to focus the particle shape and size, and then quenched with cold water.

Figure 1 shows representative transmission electron microscope (TEM) images for particles made using rhodium(II) trifluoroacetate dimer [$Rh_2(TFA)_4$], rhodium bromide ($RhBr_3$), and rhodium chloride ($RhCl_3$) in the polyol solvents ethylene glycol (EG), diethylene glycol (DEG), triethylene glycol (TREG), and tetraethylene glycol (TEG). The synthetic details and summary of results are collected in Table 1. The images presented in Figure 1 are striking: the anionic ligand largely defines the morphology, while the solvent largely defines the uniformity. $Rh_2(TFA)_4$ yields monodisperse icosahedra as the major product in EG, but higher-order polyols increase the polydispersity and other anisotropic morphologies become prevalent. Additional NaTFA increases the monodispersity (Figure 1a *vs* Supporting Information, Figure S1), but both contain fewer anisotropic impurities in EG than when larger diols are used. $RhBr_3$ yields nanocubes of increasing size for EG, DEG, and TREG. However, $RhBr_3$ in TEG yields a mixture of concave cube and branched particles. $RhCl_3$ produces branched particles in EG, but in the larger polyols yields predominantly triangular plates. For each Rh precursor

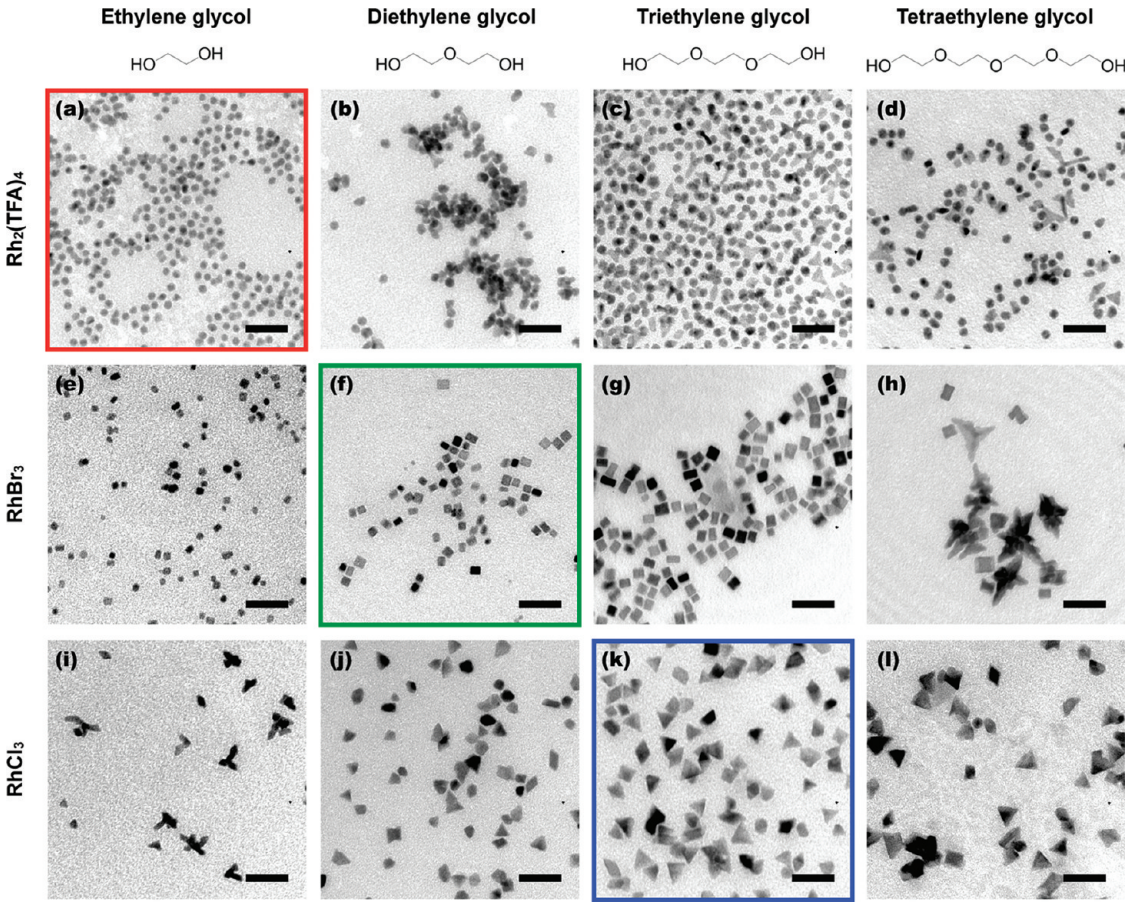

Figure 1. Representative TEM images of Rh nanoparticles synthesized using ethylene glycol, diethylene glycol, triethylene glycol, and tetraethylene glycol solvents with the reagents (a–d) $Rh_2(TFA)_4$, (e–h) $RhBr_3$, and (i–l) $RhCl_3$ (TFA = trifluoroacetate). Outlined images indicate the set of reaction conditions which results in the most monodisperse yield of Rh icosahedra (red), cubes (green), and triangular plates (blue). Scale bars are 20 nm.

TABLE 1. Summary of Reaction Conditions and Results

image number	precursor	polyol solvent	approx nucleation temp (°C)	set focusing temp (°C)	predominant (>25%) morphologies
1a	$Rh_2(TFA)_4$	EG	105–110	160	icosahedron
1b	$Rh_2(TFA)_4$	DEG	120–130	170	icosahedron
1c	$Rh_2(TFA)_4$	TREG	130–140	180	icosahedron, 3-fold branched
1d	$Rh_2(TFA)_4$	TEG	135–145	185	icosahedron, mixed anisotropic
1e	$RhBr_3$	EG	80–90	120	truncated cube
1f	$RhBr_3$	DEG	105–110	140	cube
1g	$RhBr_3$	TREG	110–120	145	cube, bar
1h	$RhBr_3$	TEG	115–125	150	concave cube, mixed concave, branched
1i	$RhCl_3$	EG	70–80	115	3-fold branched, triangular plate
1j	$RhCl_3$	DEG	85–95	130	triangular plate, spherical polyhedron
1k	$RhCl_3$	TREG	95–105	140	triangular plate
1l	$RhCl_3$	TEG	100–110	145	triangular plate, octhedron

in Figure 1, there is a corresponding polyol solvent that provides the highest yield of monodisperse products, and these samples—$Rh_2(TFA)_4$ in EG, $RhBr_3$ in DEG, and $RhCl_3$ in TREG—are highlighted with a box and used in the studies that follow.

The highest-quality icosahedra form by heating $Rh_2(TFA)_4$ in EG to a focusing temperature of 160 °C; high-resolution TEM (HRTEM), selected area electron diffraction (SAED), and size and shape distribution data for this sample are shown in Figure 2. The HRTEM image in Figure 2a shows polycrystalline multiply twinned particles, and the HRTEM images in Figure 2b,c,d show particle orientations that highlight the 5-fold, 2-fold, and 3-fold axes of an icosahedron. The lattice fringes correspond to 0.22 nm, which matches well with the (111) plane of Rh. The SAED pattern (Figure 2a, inset), with a predominant (111) reflection, is consistent with fcc-Rh as well. Statistical analysis of 342 particles indicates that

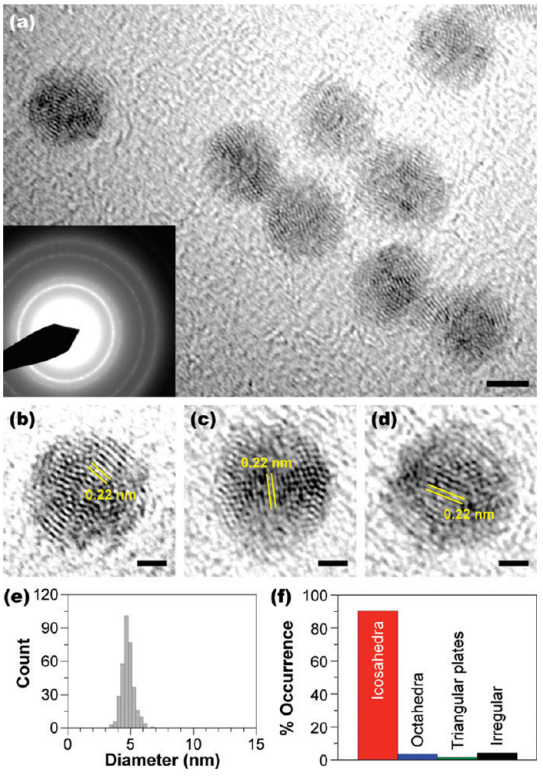

Figure 2. (a–d) HRTEM images and (a, inset) representative SAED pattern of Rh icosahedra, including isolated particles that highlight the (b) 5-fold, (c) 2-fold, and (d) 3-fold symmetry axes of an icosahedron. (e) Size distribution histogram corresponding to an average particle size of 4.8 ± 0.5 nm. (f) Summary of particle counting statistics that indicate a 90% yield of icosahedra. Scale bars are (a) 2 and (b–d) 1 nm.

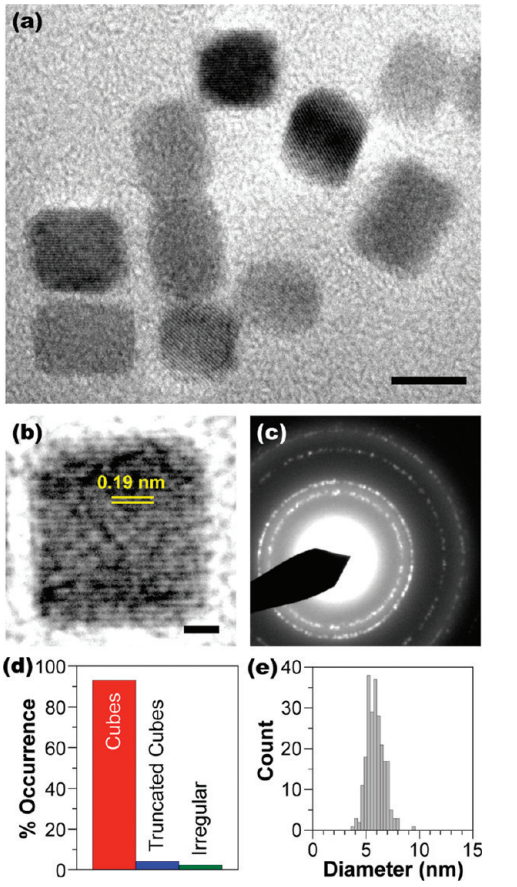

Figure 3. (a,b) HRTEM images of Rh cubes and (c) corresponding SAED pattern. Particle counting analysis indicated (d) a 93% yield of cubes with (e) a size distribution histogram showing an average body diagonal length of 5.9 ± 0.8 nm. Scale bars are (a) 5 and (b) 1 nm.

90% of the sample contains monodisperse icosahedra with an average diameter of 4.8 ± 0.5 nm (Figure 2e,f). Monodisperse Rh icosahedra synthesized in high yield have not been previously reported.

$RhBr_3$ produced nanocubes in EG, DEG, and TREG, with the highest quality cubes (based on uniform edge lengths and sharp corners and edges) formed in DEG (Figures 1f and 3a). The nanocubes formed in EG were smaller with truncated corners, similar to a previous report of nanocubes produced using $RhCl_3$ and EG in the presence of excess Br^-.[29] The nanocubes formed in TREG included a large number of particles with aspect ratios significantly greater than 1, which are better classified as rectangular nanobars. The HRTEM image in Figure 3b shows a nanocube viewed along the [001] zone axis and highlights lattice fringes of 0.19 nm that correspond to the (200) plane of Rh. The SAED pattern in Figure 3c correlates to fcc-Rh, and the increased intensity of the (200) reflection relative to (111) is consistent with the [001]-oriented nanocubes. Statistical analysis of 234 particles reveals a 93% yield of monodisperse cubes relative to other morphologies (Figure 3d), with an average body diagonal length of 5.9 ± 0.8 nm (Figure 3e).

The highest yield of triangular plates was formed by heating $RhCl_3$ in TREG to a focusing temperature of 140 °C (Figures 1k and 4a). To the best of our knowledge, monodisperse Rh plates synthesized in high yield have not been previously reported. The HRTEM image in Figure 4b shows lattice fringes of 0.22 nm, which corresponds to the (111) plane of fcc-Rh. The SAED pattern in Figure 4a inset is also consistent with fcc-Rh. HRTEM images showing thin stacked particles (Figures 4c–e) verify that they are planar. The morphological yield of 68% (Figure 4f) was not as high as for the icosahedra and cubes, but is comparable to the yields observed for colloidal plates of other metals, such as Pd.[52] The average size, measured from the tip to the opposite base for the largest side of 200 particles, was 10.6 ± 1.8 nm (Figure 4g).

The experiments presented above allowed us to eliminate effects from all variables that are known to influence morphology except the anionic ligand and the solvent. Within each polyol solvent system, the only variable that changes is the anion associated with the Rh cation, which allows us to draw conclusions exclusively about the influence of the anionic counterion on the formation of Rh nanoparticles. The importance of surface adsorbates, such as halides and other anions, is well established in the shape-selective synthesis

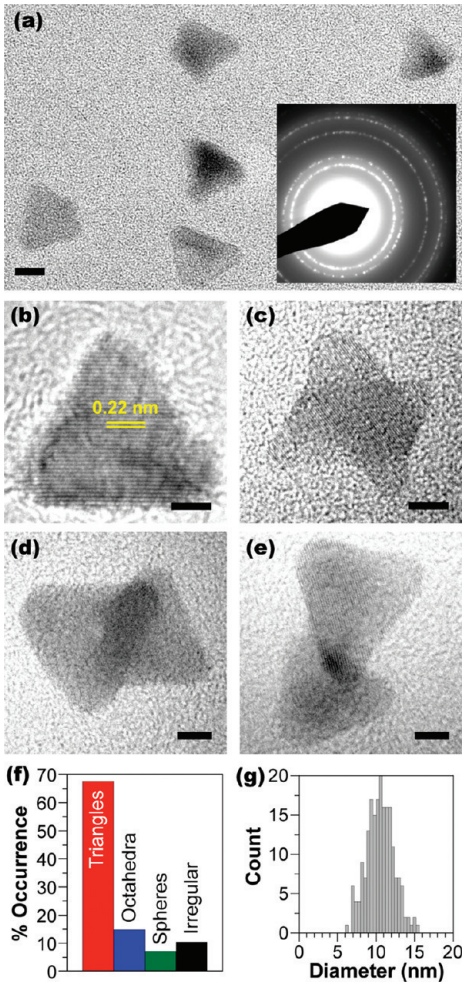

Figure 4. (a–e) HTREM images and (a, inset) corresponding SAED pattern of Rh triangular plates. Panels c–e show overlapping triangular plates, which is consistent with their planar morphology. Particle counting analysis indicated (f) a 68% yield of triangular plates with (g) a size distribution histogram showing an average particle diameter (defined from tip to opposite base) of 10.6 ± 1.8 nm. Scale bars are (a, c–e) 5 and (b) 2 nm.

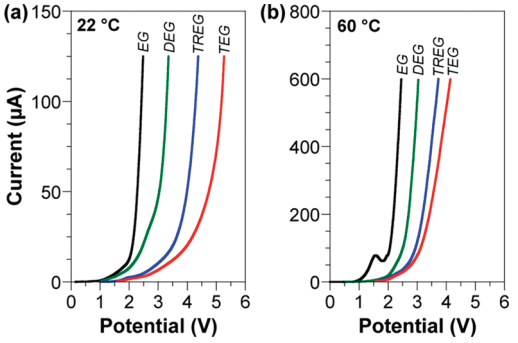

Figure 5. Linear sweep voltammograms corresponding to the oxidation of polyol solvents using a platinum working electrode at (a) room temperature and (b) at 60 °C in the presence of a 0.4 M $NaNO_3$ supporting electrolyte and using a sweep rate 10 mV/s. Higher onset potentials indicate a lower solvent oxidation potential. Potential measurements *versus* an Ag/AgCl reference electrode.

of metal nanoparticles.[53,54] For fcc metals, the surface energy (γ) follows the trend $\gamma_{(111)} < \gamma_{(100)} < \gamma_{(110)}$.[55] However, these relative energies can be modified by surface-adsorbing species, and exposed facets that would not normally be thermodynamically favored, for example, (100) planes in the case of nanocubes, can be accessed. TFA^-, as well as acetate (Supporting Information, Figure S2), passivates the {111} planes of Rh and promotes the formation of multiply twinned particles, making icosahedra the thermodynamically favored products. In the case of $RhBr_3$, Br^- selectively adsorbs to the {100} planes, as shown previously,[29] and this favors the formation of nanocubes. Like TFA^-, Cl^- from $RhCl_3$ or Na_3RhCl_6 (Supporting Information, Figure S3) also adsorbs to {111} planes, although triangular planar particles, which result from a kinetic growth regime,[56] form instead of icosahedra.

Examination of Table 1 reveals that the nucleation step, where reduction first occurs (as determined by a visual change in color to a dark brown solution and observation of small 1–2 nm seeds by HRTEM), is different for each Rh reagent in the same polyol solvent and different for each polyol solvent when using the same Rh reagent. The influence of the anion on reduction temperature, when the polyol solvent remains constant, correlates with the stability of the complex. $RhCl_3$ and $RhBr_3$ exhibit similar stability, with $RhCl_3$ being slightly less stable (thus reducing at a marginally lower temperature than $RhBr_3$). $Rh_2(TFA)_4$ is the most stable complex due to the bridging bidentate TFA^- ligand, and accordingly reduces at a significantly higher temperature than $RhCl_3$ or $RhBr_3$.

The influence of the polyol solvent on the reduction temperature correlates with its oxidation potential. Figure 5 shows linear sweep voltammetry (LSV) data for EG, DEG, TREG, and TEG at room temperature and at 60 °C. The LSV data experimentally verifies that the applied potential necessary for the onset of solvent oxidation increases, and therefore oxidation potential decreases, with the molecular size of the polyol, likely due to enhanced electronic stability of the alcohols afforded by the greater intermolecular bonding provided by the ether functionalties. Further, Figure 5b indicates that the onset potential of oxidation decreases with increasing temperature for all solvents. Therefore, the redox reaction only begins spontaneously once enough thermal energy has been provided to overcome the difference in half-reaction potentials between the metal reagent and solvent.[57] Accordingly, the larger polyols are weaker reducing agents and, with all other variables remaining constant, they will require higher temperatures to initiate reduction of Rh^{2+} or Rh^{3+}. The data presented in Table 1 are consistent with this.

Size Control of Rhodium Nanoparticle Shapes. The surface-coordinating ligand appears to largely define the nanoparticle shape, while the polyol solvent appears to help optimize monodispersity and morphological

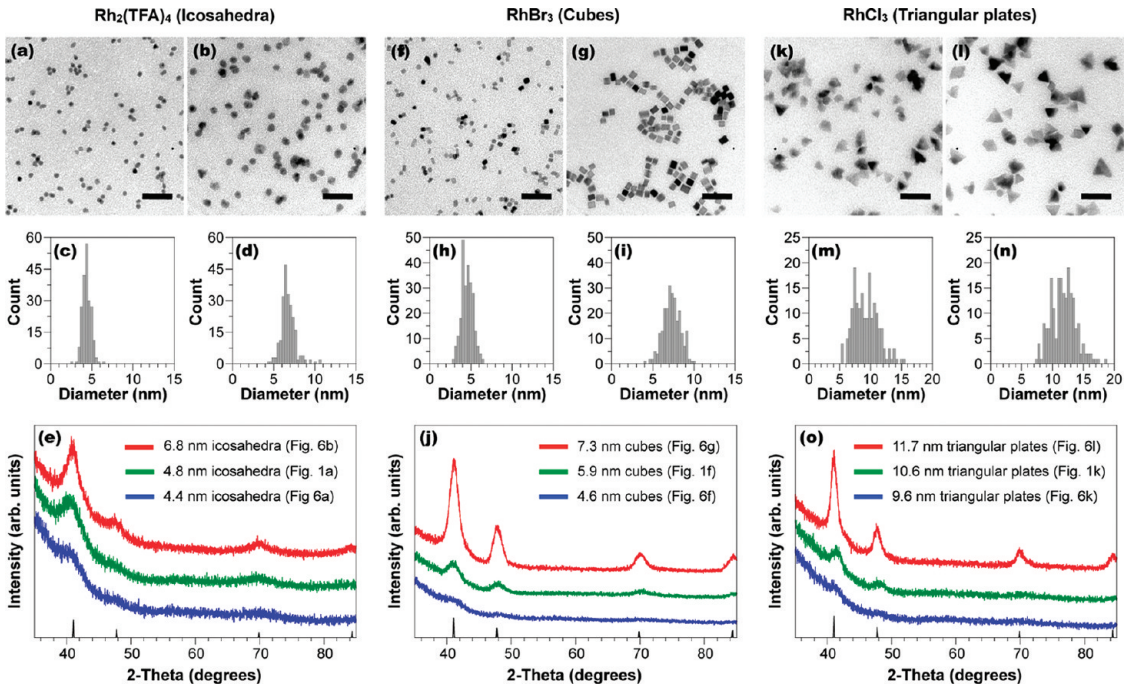

Figure 6. TEM images (top), size distribution histograms (middle), and powder XRD data (bottom) demonstrating size tunability for Rh icosahedra (a−e), cubes (f−j), and triangular plates (k−o). Size distribution histograms (c,d,h,i,m,n) confirm average particle sizes that are tunable from 4.4 ± 0.5 to 6.8 ± 0.9 nm for icosahedra, 4.6 ± 0.7 to 7.3 ± 1.0 nm for cubes, and 9.6 ± 2.5 to 11.7 ± 2.5 nm for triangular plates. Powder XRD patterns (e,j,o) for these particles, along with those from Figure 1a,f, k (which have intermediate sizes), show peak widths that increase with decreasing particle size and that correlate well with the particle sizes determined by TEM analysis. The reference Rh pattern corresponds to JCPDS card 5-0685. Scale bars are 20 nm.

yield. Superimposed upon these synthetic levers, reagent concentration can be used to tune the average nanoparticle size while maintaining the morphology and size dispersity defined by the anion and solvent. Figure 6 shows representative TEM images and size distribution histograms for Rh icosahedra, cubes, and triangular plates made using reagent concentrations less than and greater than those used to synthesize the nanoparticles shown in Figures 1−4, while leaving all other variables unchanged (*e.g.*, using the same temperatures and solvents). The nanocubes represent an ideal system in which the average size can be made larger or smaller as a function of reagent concentration: 2.5 mM $RhBr_3$ yields 4.6 ± 0.7 nm cubes, 10 mM $RhBr_3$ yields 5.9 ± 0.8 nm cubes, and 30 mM $RhBr_3$ yields 7.3 ± 1.0 nm cubes. The average size of the icosahedra also can be tuned, from 4.4 ± 0.5 nm (2 mM $Rh_2(TFA)_4$) to 6.8 ± 0.9 nm (40 mM $Rh_2(TFA)_4$), as can the triangular plates, from 9.6 ± 2.5 nm (2.5 mM $RhCl_3$) to 11.7 ± 2.5 nm (30 mM $RhCl_3$). Size tunability for the smaller icosahedra and the triangular plates was less robust than for the nanocubes, but was still successful at shifting the mean by several nanometers as a function of reagent concentration. The powder X-ray diffraction (XRD) data in Figure 6 confirm the trends in size tunability. Scherrer analysis of the (111) peaks indicates average crystallite sizes of 4.8, 5.1, and 6.9 nm for the icosahedra, 4.6, 5.9, and 7.2 nm for the cubes, and 9.2, 10.1, and 11.1 nm for the triangular plates. The plots in

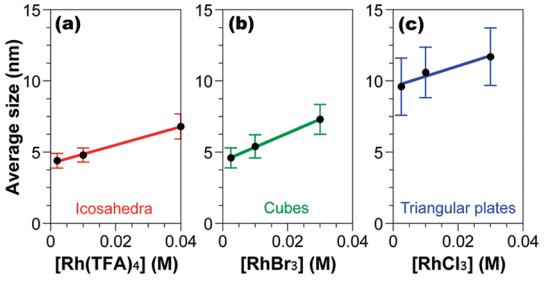

Figure 7. Plots showing the linear dependence of average particle size on the concentration of the appropriate Rh reagent for (a) icosahedra, (b) cubes, and (c) triangular plates.

Figure 7 display the linear relationship between reagent concentration and average particle size for the three shapes, which suggests that the growth is diffusion-controlled. UV−visible absorption spectroscopy indicated that the maximum wavelength of absorption due to the surface plasmon resonance (SPR) of Rh varied among particle morphologies, with peak values of approximately 250 nm for icosahedra, 255 nm for cubes, and 270 nm for triangular plates (Supporting Information, Figures S4−S7). Furthermore, the intensity of SPR absorption of Rh cubes and triangular plates increased with mean particle size, likely due to more pronounced corners and edges.[58]

Heat-Up *versus* Hot Injection Synthesis. Many polyol reactions are carried out as described above, for example, heating a homogeneous one-pot mixture of all

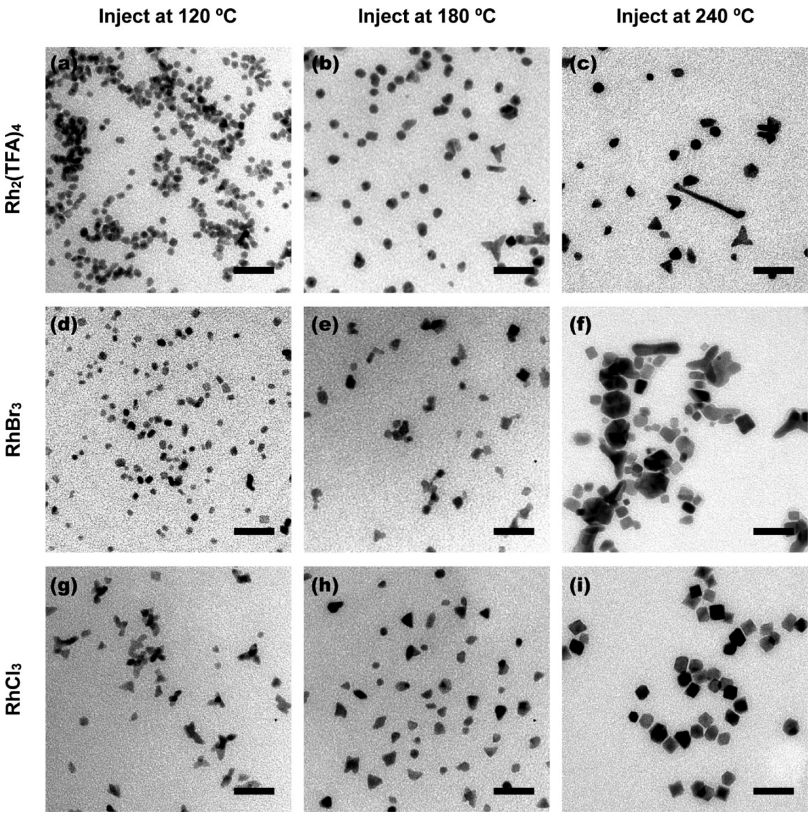

Figure 8. Representative TEM images of Rh nanoparticles synthesized by the rapid hot injection of (a–c) $Rh_2(TFA)_4$, (d–f) $RhBr_3$, and (g–i) $RhCl_3$ into polyol solvent at 120 °C (EG), 180 °C (EG), and 240 °C (TREG). Scale bars are 20 nm. The hot-injection images show similar morphological trends to the heat-up data shown in Figure 1.

dissolved reagents from room temperature to a final focusing temperature. However, an alternative approach is to inject the reagents into an already-hot solution, either rapidly or slowly with a syringe pump.[27] The studies presented above correlated product morphology and dispersity with the anion and polyol solvent. Here, a series of hot-injection experiments were used to understand whether the differences observed as a function of polyol solvent were inherently caused by the solvent itself or by the temperature at which reduction and subsequent growth occurred. $Rh_2(TFA)_4$, $RhBr_3$, and $RhCl_3$ were rapidly injected into hot polyol solvent at 120, 180, and 240 °C (Figure 8) using the same reagent concentrations that were used in Figure 1. EG was used for the injections at 120 and 180 °C and TREG was used for the 240 °C injection because of its higher boiling point. To verify that any observed differences in product size and morphology were due to temperature and not to the solvent, the Rh reagent solutions were also injected into TREG at 180 °C and compared to the samples prepared by injection into EG at 180 °C (Supporting Information, Figure S8). No significant variance was observed, indicating that while the results of the hot-injection syntheses are dependent upon temperature, they are for the most part independent of the solvent.

The trends in Rh nanoparticle morphologies shown in Figure 8 compare favorably with those presented earlier in Figure 1. For example, higher-temperature injection of $Rh_2(TFA)_4$ (the 180 and 240 °C samples in Figure 8b and 8c, respectively) produced a larger population of nonicosahedral nanoparticles than at 120 °C (Figure 8a). This is analogous to the observations in Figure 1a–d, where heating $Rh_2(TFA)_4$ in the higher-order polyols DEG, TREG, and TEG (which had higher reduction temperatures) produced a higher population of nonicosahedral particles. Likewise, injection of $RhBr_3$ into EG at 120 °C (Figure 8d) produced particles with cube and truncated cube morphologies in 80% yield (analogous to the polyols that facilitated reduction at lower temperatures in Figure 1e–g), while higher-temperature injections produced more anisotropic and polydisperse particles (Figures 1h and 8e,f). Finally, hot injection of $RhCl_3$ produced 3-fold branched particles at the lowest temperature (Figure 8g), mostly triangular plates at the medium temperature (Figure 8h), and predominantly octahedral particles at the highest temperature (Figure 8i). Again, this is analogous to the trends observed in Figure 1i–l, where the solvent with the lowest reduction temperature generated branched particles (Figure 1i), moderate reduction temperatures yielded triangular plates (Figure 1j,k), and higher temperatures produced a mixture that is mostly triangular plates and octahedra (Figure 1l).

The data in Figures 1 and 8 together indicate that, for a given Rh precursor, the temperature at which particle formation takes place is the primary determinant of variability in morphology and dispersity. We attribute this to the influence of temperature on the kinetics of precursor reduction and nanoparticle growth. For example, hot injection at 120 °C typically requires 10−15 s for reduction to occur, while reduction is almost instantaneous at 240 °C. This is the same for the heat-up method: solvents that facilitate lower-temperature reduction reduce at a much slower rate than those that require higher temperatures to initiate reduction.

The reaction rate, which is a function of the temperature at which reduction occurs, regardless of the method,[59] controls how quickly seeds are produced and determines whether growth occurs under thermodynamic conditions, where equilibrium shapes form, or under kinetic conditions, where different morphologies are accessible. It is well-known that anisotropic morphologies, such as rods and branched structures, form when reaction conditions favor kinetic control, where particle growth occurs either very rapidly (*e.g.*, at high temperature) or very slowly (*e.g.*, relatively low temperatures or gradual addition of reagents using a syringe pump).[60] Such conditions favor monomer addition to the highest-energy facets of a seed (*e.g.*, corners and edges) rather than epitaxial growth across the entire particle. Particularly fast reduction, for example, at high temperatures, tends to yield greater morphological diversity because kinetic control predominates over thermodynamic control and there is little separation between the stages of seed nucleation and particle growth.[34,61]

Similarly, particularly slow reduction tends to yield a reactive monomer concentration that is too low, which promotes growth at selected sites on a seed particle, for example, high-energy locations such as corners and vertices. Xia and co-workers have synthesized 3-fold or 5-fold branched Rh nanoparticles by the slow addition of $RhCl_3$ or $Rh_2(TFA)_4$ with a syringe pump into a hot solvent.[35,36] In our system, fast injection of $RhCl_3$ into a lower-temperature solvent produced similarly branched nanoparticles (Figure 8g) facilitated by slower reaction kinetics and indicating that an *in situ* gradual addition of monomer occurred. Alternatively, reduction by the heat-up method at relatively low temperatures using $RhCl_3$ in EG (Figure 1i) or $Rh_2(TFA)_4$ in 1,3-propanediol (PDO) (Supporting Information, Figure S9), which has a higher oxidation potential than EG and therefore facilitates lower-temperature reduction, also produces 3-fold or 5-fold branched nanoparticles. This suggests that lower-temperature reduction and gradual reagent addition are equivalent strategies for achieving kinetically controlled growth.

These results and observations imply that, in order to access monodisperse isotropic particles, a moderate rate of precursor reduction is essential. The thermal conditions corresponding to a "moderate" rate will vary for each system, but the choice of polyol solvent allows for tunability of the reduction temperature and subsequent reaction rate, therefore facilitating optimization of particle quality and uniformity. This is in addition to the impact of separating the nucleation and growth stages, which is also known to be essential in the formation of uniform particles.[62]

Application: Synthesis of Rhodium Octahedra. In Figure 1l, where $RhCl_3$ was reduced with TEG by gradual heating, octahedra were observed as a minority product. In Figure 8i, where $RhCl_3$ was injected directly into TREG at 240 °C, octahedra became the majority product, although still in relatively low morphological purity relative to other shapes that include cubooctahedra and truncated octahedra. The observations and analyses outlined in the previous section suggest that optimization of quality and morphological purity should be achievable by selecting a polyol solvent that reduces Rh^{3+} to Rh^0 at a high temperature (since octahedra formed in the highest-temperature injection study) and that has a high reflux temperature in order to effectively separate nucleation and growth. Poly(ethylene glycol) with an average molecular weight of 300 (PEG 300) has 2−3 additional ethylene oxide groups per molecule compared to TEG, based on the molecular weights, and a reflux temperature that is higher (~325 °C). When $RhCl_3$ is dissolved with PVP in PEG 300 and heated, the solution begins turning darker around 130 °C. However, the color change that is indicative of growth (*e.g.*, formation of a dark brown or black-colored solution) only occurs at approximately 190 °C, which is significantly higher than in the lower-order polyols.

Figure 9a shows a representative TEM image of the octahedra, which form in approximately 70% morphological yield and have an average width of 6.7 ± 1.0 nm. The SAED pattern in Figure 9b and powder XRD pattern in Supporting Information, Figure S10 are consistent with fcc-Rh. The HRTEM image in Figure 9c shows that the octahedra are single crystals with lattice fringes of 0.22 nm, which corresponds to the (111) plane of Rh. The UV−visible absorption spectrum (Supporting Information, Figure S11) indicates that the SPR absorption peak lies at 245 nm. Octahedra of other noble metals, such as Au, Ag, Pt, and Pd, are known, but this represents the first report of Rh octahedra synthesized without the assistance of additional metals.[31] While triangular plates, which are the predominant product formed using medium-order polyols, were not observed upon heating $RhCl_3$ in PEG 300, the presence of exposed {111} facets is consistent with the hypothesis that the Cl^- anion preferentially stabilizes {111} planes. This affirms that for the $RhCl_3$ system at high reduction temperatures octahedra are favored, at intermediate temperatures triangular plates are favored, and at low temperatures 3-fold branched particles are

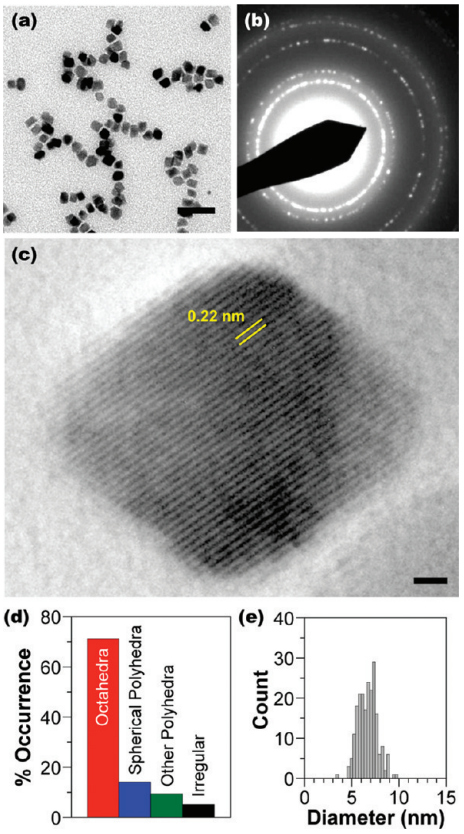

Figure 9. (a) TEM image, (b) SAED pattern, and (c) HRTEM image of Rh octahedra synthesized by reducing $RhCl_3$ in PEG 300. Particle counting analysis indicated (d) a 70% yield of octahedra with (e) a size distribution histogram showing an average diameter of 6.7 ± 1.0 nm. Scale bars are (a) 20 and (c) 1 nm.

favored. These correspond to the thermodynamic, isotropic kinetic, and anisotropic kinetic products, respectively, and variation of the reducing solvent can selectively and predictably yield any of these three morphologies.

CONCLUSIONS

Four distinct morphologies of monodisperse Rh nanoparticles have been synthesized in high yield using a simple one-pot polyol heat-up method. These include nanoscale cubes, octahedra, icosahedra, and triangular plates, the latter two of which have not been previously reported. Surface-coordinating ligands define the thermodynamically favored nanoparticle facets and morphology, while the choice of polyol solvent helps to fine-tune the uniformity through modulation of the growth kinetics. Furthermore, the mean sizes of these particles can be tuned by manipulating the starting concentration of the metal reagent. These results provide empirical guidelines for synthesizing Rh nanoparticles, which are expected to facilitate the direct comparison of their properties as a function of shape and size in catalytic and electrocatalytic applications.

More generally, these results collectively uncover a new strategy for improving the synthesis of monodisperse metal nanoparticles. Each polyol solvent has a different oxidation potential, and this defines the temperature at which particle formation occurs. Judicious polyol solvent selection, which permits tuning of the particle formation temperature, is the primary synthetic lever for manipulating the rate of particle growth and for determining whether particles form in a kinetic or thermodynamic growth regime. To obtain the highest-quality isotropic particles, a moderate growth rate is desirable. Importantly, these results use polyol solvent selection to merge two commonly used nanoparticle synthesis strategies: the one-pot heat-up method and the syringe pump hot-injection method. The syringe pump method continuously delivers small, controlled amounts of reagent, which facilitates kinetically controlled growth to yield products that often have complex morphologies and represent nonequilibrium nanostructures. By using different polyol solvents, similar kinetic products can be obtained using simple one-pot heat-up methods, as well as thermodynamic products with superior monodispersity facilitated by the deliberate separation of the nucleation and growth steps. While Rh nanoparticles were the focus of these studies, the concepts should be applicable to other metal nanoparticle systems made using polyol processes.

EXPERIMENTAL SECTION

Materials. Rhodium(III) chloride hydrate ($RhCl_3 \cdot xH_2O$, Rh 38.5−45.5%), rhodium(III) bromide hydrate ($RhBr_3 \cdot xH_2O$), sodium hexachlororhodate(III) dodecahydrate ($Na_3RhCl_6 \cdot 12H_2O$, Rh 17.1%), rhodium(II) acetate dimer [$Rh_2(COOCH_3)_4$, Rh 46.2% min], diethylene glycol (99%), tetraethylene glycol (99%), and 1,3-propanediol (99%) were purchased from Alfa Aesar. Rhodium(II) trifluoroacetate dimer [$Rh_2(COOCF_3)_4$, 98%], sodium trifluoroacetate ($NaCOOCF_3$, 98%), sodium nitrate (>99%), and poly(ethylene glycol) MW = 300 (PEG 300) were purchased from Sigma-Aldrich. Ethylene glycol (>99%) was purchased from J. T. Baker. Triethylene glycol (>99%) was purchased from Fluka. Poly(vinyl pyrrolidone) (PVP) average MW = 40 000 was purchased from TCI. Solvents, including acetone, ethanol, and hexanes, were of analytical grade. All chemicals were used as received.

Synthesis. In a typical synthesis, Rh reagent (0.1 mmol by Rh atom) and PVP stabilizer (2 mmol by repeating unit) were dissolved in 10 mL of polyol solvent using a sonic bath or, in the case of higher-order solvents, a 65 °C water bath. For the synthesis of Rh icosahedra, $NaCOOCF_3$ [8:1 ratio with $Rh_2(COOCF_3)_4$] was also added. The solution was stirred vigorously

under bubbling argon in a 25 mL three-neck flask fitted with a condenser. Temperature was maintained using a digital controller with glass-coated thermocouple (Gemini, J-KEM Scientific) and 25 mL heating mantle (Glas-Col). The solution was heated to a certain temperature where particle nucleation began, as evidenced by a darkening of the solution color. After holding at these conditions for 15 min, the solution was heated to a focusing temperature, causing the solution color to darken further, and maintained there for 1.5 h before being quenched with a cold water bath.

To produce particles of larger average size the amount of reagent and stabilizer was increased by 3−4 times, and to produce particles of smaller average size the amount of polyol solvent was increased by 4−5 times. For hot injections, the reagent and stabilizer were dissolved in 3 mL of solvent and then injected rapidly through a septum into 7 mL of solvent held at the desired temperature under bubbling argon, and maintained for 1.5 h before quenching with cold water bath. Once at room temperature, all reaction solutions were diluted by adding three times the volume of acetone. For larger-order polyols, 5−10 mL of hexanes was also added. Particles were separated from polyol solvents and excess reagents by centrifugation at 10000 rpm for 3 min and redispersed in ethanol with a sonic bath. Excess hexanes were added and the particles were separated twice more by centrifugation at 5000 rpm for 3 min before being stored dispersed in ethanol.

Characterization. Transmission electron microscopy (TEM) images were obtained from a JEOL 1200 EX II microscope operating at 80 kV. High-resolution TEM (HRTEM) images and selected area electron diffraction (SAED) patterns were collected using a JEOL-2010 LaB_6 microscope operating at 200 kV. Samples were prepared by casting one drop of nanoparticles dispersed in ethanol onto a Formvar and carbon-coated copper grid. Powder X-ray diffraction (XRD) data were collected by a Bruker Advance D8 X-ray diffractometer using Cu Kα radiation. Linear sweep voltammetry (LSV) was performed with a Princeton Applied Research VersaSTAT 3 potentiostat at a sweep rate of 10 mV/s using a Pt working electrode, Ag/AgCl reference electrode, Pt counter-electrode, and 0.4 M $NaNO_3$ supporting electrolyte. UV−visible spectroscopy data were collected using an Ocean Optics HR4000 spectrometer using a DH-2000-BAL light source and quartz cuvettes. Particle counting analysis used a minimum of 200 individual particles, and size was determined using the ImageJ program (http://rsbweb.nih.gov/ij/).

Acknowledgment. This work was supported by the National Science Foundation (NSF DMR-0748943). Electron microscopy was performed at the Electron Microscopy Facility at the Huck Institutes of the Life Sciences and at the Materials Characterization Facility of the Penn State Materials Research Institute.

Supporting Information Available: UV−visible absorption spectra of Rh nanoparticles, powder XRD pattern of Rh octahedra, and additional TEM images. This material is available free of charge *via* the Internet at http://pubs.acs.org.

REFERENCES AND NOTES

1. Jia, C.-J.; Schuth, F. Colloidal Metal Nanoparticles as a Component of Designed Catalyst. *Phys. Chem. Chem. Phys.* **2011**, *13*, 2457–2487.
2. Jain, P. K.; Huang, X.; El-Sayed, I. H.; El-Sayed, M. A. Noble Metals on the Nanoscale: Optical and Photothermal Properties and Some Applications in Imaging, Sensing, Biology, and Medicine. *Acc. Chem. Res.* **2008**, *41*, 1578–1586.
3. El-Sayed, M. A. Some Interesting Properties of Metals Confined in Time and Nanometer Space of Different Shapes. *Acc. Chem. Res.* **2001**, *34*, 257–264.
4. Behrens, S. Preparation of Functional Magnetic Nanocomposites and Hybrid Materials: Recent Progress and Future Directions. *Nanoscale* **2011**, *3*, 877–892.
5. Talapin, D. V.; Lee, J.-S.; Kovalenko, M. V.; Shevchenko, E. V. Prospects of Colloidal Nanocrystals for Electronic and Optoelectronic Applications. *Chem. Rev.* **2009**, *110*, 389–458.
6. Xia, Y.; Xiong, Y.; Lim, B.; Skrabalak, S. E. Shape-Controlled Synthesis of Metal Nanocrystals: Simple Chemistry Meets Complex Physics? *Angew Chem., Int. Ed.* **2009**, *48*, 60–103.
7. Tao, A. R.; Habas, S.; Yang, P. Shape Control of Colloidal Metal Nanocrystals. *Small* **2008**, *4*, 310–325.
8. Milligan, W. O.; Morriss, R. H. Morphology of Colloidal Gold—A Comparative Study. *J. Am. Chem. Soc.* **1964**, *86*, 3461–3467.
9. Zhang, J.; Yang, H.; Fang, J.; Zou, S. Synthesis and Oxygen Reduction Activity of Shape-Controlled Pt_3Ni Nanopolyhedra. *Nano Lett.* **2010**, *10*, 638–644.
10. Lee, I.; Delbecq, F.; Morales, R.; Albiter, M. A.; Zaera, F. Tuning Selectivity in Catalysis by Controlling Particle Shape. *Nat. Mater.* **2009**, *8*, 132–138.
11. Tsung, C.-K.; Kuhn, J. N.; Huang, W.; Aliaga, C.; Hung, L.-I.; Somorjai, G. A.; Yang, P. Sub-10 nm Platinum Nanocrystals with Size and Shape Control: Catalytic Study for Ethylene and Pyrrole Hydrogenation. *J. Am. Chem. Soc.* **2009**, *131*, 5816–5822.
12. Wu, J.; Gross, A.; Yang, H. Shape and Composition-Controlled Platinum Alloy Nanocrystals Using Carbon Monoxide as Reducing Agent. *Nano Lett.* **2011**, *11*, 798–802.
13. Somorjai, G. A.; Blakely, D. W. Mechanism of Catalysis of Hydrocarbon Reactions by Platinum Surfaces. *Nature* **1975**, *258*, 580–583.
14. Tian, N.; Zhou, Z.-Y.; Sun, S.-G.; Ding, Y.; Wang, Z. L. Synthesis of Tetrahexahedral Platinum Nanocrystals with High-Index Facets and High Electro-oxidation Activity. *Science* **2007**, *316*, 732–735.
15. Wang, C.; Daimon, H.; Onodera, T.; Koda, T.; Sun, S. A General Approach to the Size- and Shape-Controlled Synthesis of Platinum Nanoparticles and Their Catalytic Reduction of Oxygen. *Angew. Chem., Int. Ed.* **2008**, *47*, 3588–3591.
16. Kyriakou, G.; Beaumont, S. K.; Humphrey, S. M.; Antonetti, C.; Lambert, R. M. Sonogashira Coupling Catalyzed by Gold Nanoparticles: Does Homogeneous or Heterogeneous Catalysis Dominate? *ChemCatChem* **2010**, *2*, 1444–1449
17. Campbell, C. T.; Parker, S. C.; Starr, D. E. The Effect of Size-Dependent Nanoparticle Energetics on Catalyst Sintering. *Science* **2002**, *298*, 811–814.
18. Joo, S. H.; Park, J. Y.; Renzas, J. R.; Butcher, D. R.; Huang, W.; Somorjai, G. A. Size Effect of Ruthenium Nanoparticles in Catalytic Carbon Monoxide Oxidation. *Nano Lett.* **2010**, *10*, 2709–2713.
19. Grass, M. E.; Zhang, Y.; Butcher, D. R.; Park, J. Y.; Li, Y.; Bluhm, H.; Bratlie, K. M.; Zhang, T.; Somorjai, G. A. A Reactive Oxide Overlayer on Rhodium Nanoparticles during CO Oxidation and Its Size Dependence Studied by *in Situ* Ambient-Pressure X-ray Photoelectron Spectroscopy. *Angew. Chem., Int. Ed.* **2008**, *47*, 8893–8896.
20. Cimpeanu, V.; Kočevar, M.; Parvulescu, V. I.; Leitner, W. Preparation of Rhodium Nanoparticles in Carbon Dioxide Induced Ionic Liquids and Their Application to Selective Hydrogenation. *Angew. Chem., Int. Ed.* **2009**, *48*, 1085–1088.
21. McClure, S. M.; Lundwall, M. J.; Goodman, D. W. Planar Oxide Supported Rhodium Nanoparticles as Model Catalysts. *Proc. Natl. Acad. Sci., U.S.A.* **2011**, *108*, 931–936.
22. Kanuru, V. K.; Humphrey, S. M.; Kyffin, J. M. W.; Jefferson, D. A.; Burton, J. W.; Armbruster, M.; Lambert, R. M. Evidence for Heterogeneous Sonogashira Coupling of Phenylacetylene and Iodobenzene Catalyzed by Well Defined Rhodium Nanoparticles. *Dalton Trans.* **2009**, 7602–7605.
23. Hernandez, L.; Nord, F. F. Interpretation of the Mechanism of Catalytic Reductions with Colloidal Rhodium in the Liquid Phase. *J. Colloid Sci.* **1948**, *3*, 363–375.
24. Hirai, H.; Nakao, Y.; Toshima, N.; Adachi, K. Colloidal Rhodium in Poly(vinyl alcohol) as a Hydrogenation Catalyst of Olefins. *Chem. Lett.* **1976**, *5*, 905–10.
25. Hirai, H.; Nakao, Y.; Toshima, N. Colloidal Rhodium in Poly-(vinylpyrrolidone) as Hydrogenation Catalyst for Internal Olefins. *Chem. Lett.* **1978**, *7*, 545–8.
26. Zhang, Y.; Grass, M. E.; Habas, S. E.; Tao, F.; Zhang, T.; Yang, P.; Somorjai, G. A. One-Step Polyol Synthesis and Langmuir−Blodgett Monolayer Formation of Size-Tunable Monodisperse Rhodium Nanocrystals with Catalytically Active (111) Surface Structures. *J. Phys. Chem. C* **2007**, *111*, 12243–12253.
27. Humphrey, S. M.; Grass, M. E.; Habas, S. E.; Niesz, K.; Somorjai, G. A.; Tilley, T. D. Rhodium Nanoparticles from Cluster Seeds:

Control of Size and Shape by Precursor Addition Rate. *Nano Lett.* **2007**, *7*, 785–790.
28. Jang, K.; Kim, H. J.; Son, S. U. Low-Temperature Synthesis of Ultrathin Rhodium Nanoplates *via* Molecular Orbital Symmetry Interaction between Rhodium Precursors. *Chem. Mater.* **2010**, *22*, 1273–1275.
29. Zhang, Y.; Grass, M. E.; Kuhn, J. N.; Tao, F.; Habas, S. E.; Huang, W.; Yang, P.; Somorjai, G. A. Highly Selective Synthesis of Catalytically Active Monodisperse Rhodium Nanocubes. *J. Am. Chem. Soc.* **2008**, *130*, 5868–5869.
30. Park, K. H.; Jang, K.; Kim, H. J.; Son, S. U. Near-Monodisperse Tetrahedral Rhodium Nanoparticles on Charcoal: The Shape-Dependent Catalytic Hydrogenation of Arenes. *Angew. Chem., Int. Ed.* **2007**, *46*, 1152–1155.
31. Long, N. V.; Chien, N. D.; Hirata, H.; Matsubara, T.; Ohtaki, M.; Nogami, M. Highly Monodisperse Cubic and Octahedral Rhodium Nanocrystals: Their Evolutions from Sharp Polyhedrons into Branched Nanostructures and Surface-Enhanced Raman Scattering. *J. Cryst. Growth* **2011**, *320*, 78–89.
32. Ewers, T. D.; Sra, A. K.; Norris, B. C.; Cable, R. E.; Cheng, C.-H.; Shantz, D. F.; Schaak, R. E. Spontaneous Hierarchical Assembly of Rhodium Nanoparticles into Spherical Aggregates and Superlattices. *Chem. Mater.* **2005**, *17*, 514–520.
33. Yuan, Q.; Zhou, Z.; Zhuang, J.; Wang, X. Tunable Aqueous Phase Synthesis and Shape-Dependent Electrochemical Properties of Rhodium Nanostructures. *Inorg. Chem.* **2010**, *49*, 5515–5521.
34. Zhang, H.; Li, W.; Jin, M.; Zeng, J.; Yu, T.; Yang, D.; Xia, Y. Controlling the Morphology of Rhodium Nanocrystals by Manipulating the Growth Kinetics with a Syringe Pump. *Nano Lett.* **2011**, *11*, 898–903.
35. Zettsu, N.; McLellan, J. M.; Wiley, B.; Yin, Y.; Li, Z.-Y.; Xia, Y. Synthesis, Stability, and Surface Plasmonic Properties of Rhodium Multipods, and Their Use as Substrates for Surface-Enhanced Raman Scattering. *Angew. Chem., Int. Ed.* **2006**, *45*, 1288–1292.
36. Zhang, H.; Xia, X.; Li, W.; Zeng, J.; Dai, Y.; Yang, D.; Xia, Y. Facile Synthesis of Five-fold Twinned, Starfish-like Rhodium Nanocrystals by Eliminating Oxidative Etching with a Chloride-free Precursor. *Angew. Chem., Int. Ed.* **2010**, *49*, 5296–5300.
37. Zhang, Y.; Grass, M. E.; Huang, W.; Somorjai, G. A. Seedless Polyol Synthesis and CO Oxidation Activity of Monodisperse (111)- and (100)-Oriented Rhodium Nanocrystals in Sub-10 nm Sizes. *Langmuir* **2010**, *26*, 16463–16468.
38. Grzelczak, M.; Perez-Juste, J.; Mulvaney, P.; Liz-Marzan, L. M. Shape Control in Gold Nanoparticle Synthesis. *Chem. Soc. Rev.* **2008**, *37*, 1783–1791.
39. Wiley, B.; Sun, Y.; Xia, Y. Synthesis of Silver Nanostructures with Controlled Shapes and Properties. *Acc. Chem. Res.* **2007**, *40*, 1067–1076.
40. Chen, J.; Lim, B.; Lee, E. P.; Xia, Y. Shape-Controlled Synthesis of Platinum Nanocrystals for Catalytic and Electrocatalytic Applications. *Nano Today* **2009**, *4*, 81–95.
41. Xiong, Y.; Xia, Y. Shape-Controlled Synthesis of Metal Nanostructures: The Case of Palladium. *Adv. Mater.* **2007**, *19*, 3385–3391.
42. Fievet, F.; Lagier, J. P.; Blin, B.; Beaudoin, B.; Figlarz, M. Homogeneous and Heterogeneous Nucleations in the Polyol Process for the Preparation of Micron and Submicron Size Metal Particles. *Solid State Ionics* **1989**, *32—33*, 198–205.
43. Fievet, F.; Lagier, J. P.; Figlarz, M. Preparing Monodisperse Metal Powers in Micrometer and Submicrometer Sizes by the Polyol Process. *MRS Bull.* **1989**, *14*, 29–34.
44. Ducamp-Sanguesa, C.; Herrera-Urbina, R.; Figlarz, M. Synthesis and Characterization of Fine and Monodisperse Silver Particles of Uniform Shape. *J. Solid State Chem.* **1992**, *100*, 272–280.
45. Sun, Y.; Xia, Y. Shape-Controlled Synthesis of Gold and Silver Nanoparticles. *Science* **2002**, *298*, 2176–2179.
46. Kim, F.; Connor, S.; Song, H.; Kuykendall, T.; Yang, P. Platonic Gold Nanocrystals. *Angew. Chem., Int. Ed.* **2004**, *43*, 3673–3677.
47. Cai, W.; Wan, J. Facile Synthesis of Superparamagnetic Magnetite Nanoparticles in Liquid Polyols. *J. Colloid Interface Sci.* **2007**, *305*, 366–370.
48. Park, K. H.; Im, S. H.; Park, O. O. The Size Control of Silver Nanocrystals with Different Polyols and its Application to Low-Reflection Coating Materials. *Nanotechnology* **2011**, *22*, 045602.
49. Carroll, K. J.; Reveles, J. U.; Shultz, M. D.; Khanna, S. N.; Carpenter, E. E. Preparation of Elemental Cu and Ni Nanoparticles by the Polyol Method: An Experimental and Theoretical Approach. *J. Phys. Chem. C* **2011**, *115*, 2656–2664.
50. Yan, X.; Liu, H.; Liew, K. Y. Size Control of Polymer-Stabilized Ruthenium Nanoparticles by Polyol Reduction. *J. Mater. Chem.* **2001**, *11*, 3387–3391.
51. Xiong, Y.; Chen, J.; Wiley, B.; Xia, Y.; Aloni, S.; Yin, Y. Understanding the Role of Oxidative Etching in the Polyol Synthesis of Pd Nanoparticles with Uniform Shape and Size. *J. Am. Chem. Soc.* **2005**, *127*, 7332–7333.
52. Xiong, Y.; McLellan, J. M.; Chen, J.; Yin, Y.; Li, Z.-Y.; Xia, Y. Kinetically Controlled Synthesis of Triangular and Hexagonal Nanoplates of Palladium and Their SPR/SERS Properties. *J. Am. Chem. Soc.* **2005**, *127*, 17118–17127.
53. Filankembo, A.; Giorgio, S.; Lisiecki, I.; Pileni, M. P. Is the Anion the Major Parameter in the Shape Control of Nanocrystals? *J Phys. Chem. B* **2003**, *107*, 7492–7500.
54. Im, S. H.; Lee, Y. T.; Wiley, B.; Xia, Y. Large-Scale Synthesis of Silver Nanocubes: The Role of HCl in Promoting Cube Perfection and Monodispersity. *Angew. Chem., Int. Ed.* **2005**, *44*, 2154–2157.
55. Wang, Z. L. Transmission Electron Microscopy of Shape-Controlled Nanocrystals and Their Assemblies. *J. Phys. Chem. B* **2000**, *104*, 1153–1175.
56. Lim, B.; Jiang, M.; Tao, J.; Camargo, P. H. C.; Zhu, Y.; Xia, Y. Shape-Controlled Synthesis of Pd Nanocrystals in Aqueous Solutions. *Adv. Funct. Mater.* **2009**, *19*, 189–200.
57. Bonet, F.; Guéry, C.; Guyomard, D.; Herrera Urbina, R.; Tekaia-Elhsissen, K.; Tarascon, J. M. Electrochemical Reduction of Noble Metal Compounds in Ethylene Glycol. *Int. J. Inorg. Mater.* **1999**, *1*, 47–51.
58. Lu, X.; Rycenga, M.; Skrabalak, S. E.; Wiley, B.; Xia, Y. Chemical Synthesis of Novel Plasmonic Nanoparticles. *Annu. Rev. Phys. Chem.* **2009**, *60*, 167–192.
59. Timonen, J. V. I.; Seppälä, E. T.; Ikkala, O.; Ras, R. H. A. From Hot-Injection Synthesis to Heating-Up Synthesis of Cobalt Nanoparticles: Observation of Kinetically Controllable Nucleation. *Angew. Chem., Int. Ed.* **2011**, *50*, 2080–2084.
60. Lim, B.; Xia, Y. Metal Nanocrystals with Highly Branched Morphologies. *Angew. Chem., Int. Ed.* **2011**, *50*, 76–85.
61. Xiong, Y.; Cai, H.; Wiley, B. J.; Wang, J.; Kim, M. J.; Xia, Y. Synthesis and Mechanistic Study of Palladium Nanobars and Nanorods. *J. Am. Chem. Soc.* **2007**, *129*, 3665–3675.
62. Sugimoto, T. Preparation of Monodispersed Colloidal Particles. *Adv. Colloid Interface Sci.* **1987**, *28*, 65–108.